To appear in the Astrophysical Journal, Supplement Series

THE CALIBRATION OF THE *ROSAT* HRI PARTICLE BACKGROUND

S. L. Snowden
Code 662, NASA/Goddard Space Flight Center, Greenbelt, MD 20771
Universities Space Research Association.

ABSTRACT

A calibration for the particle background (PB) of the *ROSAT* High Resolution Imager (HRI) is presented. It is found that the PB rate is temporally a relatively stable function of the subsatellite geographic position, and that the average master veto (MV) signal of the Position Sensitive Proportional Counter is a good template of that function. By determining the general correlation between the average MV signal and PB rate as a function of time, and scaling the general correlation by an individual observation's light curve, an accurate PB model for that observation can be produced.

Detector maps for the distribution of PB events and the distribution of exposure (including vignetting, detector artifacts, and quantum efficiency variations) are also presented. The maps were created from Earth-block data collected throughout the mission.

Subject headings: instrumentation: detectors — methods: data analysis, observational — space vehicles — X-rays: general

1. INTRODUCTION

The *ROSAT* (Trümper 1983;92) High Resolution Imager (HRI, Zombeck et al. 1995; David et al. 1997) is similar to the *Einstein* HRI (Kellogg et al. 1976; Henry et al. 1977; Henry & Henriksen 1986) and consists of two cascaded microchannel plates (MCPs, see Fraser 1989) which provide excellent angular resolution ($\sim 5''$) for the detection of cosmic X-rays. A cosmic X-ray enters a channel in the MCP and photoionizes an atom on the wall (coated with a CsI photocathode). With an applied voltage, the channel then acts as a small photomultiplier tube producing a final charge pulse which is detected. However, any other ionization along the channel wall, including any induced by a cosmic-ray event, will also produce a charge pulse and be detected. Because the HRI lacks an efficient mechanism for the vetoing of spurious events caused by cosmic rays, the residual particle background (PB) in the accepted data is rather high, five to ten times the intensity of the cosmic diffuse background (compared to $1-2\%$ for the *ROSAT* Position Sensitive Proportional Counter, PSPC, Pfeffermann et al. 1987 as determined by Snowden et al. 1992).

While the study of point sources is relatively unaffected by the PB, it is of critical importance when considering observations of extended objects which cover large regions of the detector field of view. (See Snowden et al. 1994b and references therein for an extensive discussion of the subject for PSPC observations.) Since a major goal of such observations is to compare the surface brightness variations of the emission regions, it is vital to correct the data to a uniform zero level and sensitivity across the field. Since the distribution of PB counts (relatively flat) across the detector is different than that for focussed X-rays (vignetted by the telescope), the apparent large-angle structure across the field is affected. The study of extended structures requires a detailed correction for vignetting and any variation in the quantum efficiency of the detector. Thus, one must have a reliable method for casting both the effective exposure and modeled PB events into sky coordinates.

Section 2 of this paper presents a method for modeling the temporal variation of the particle background. Section 3 details the creation of detector maps for the particle background and effective exposure. Section 4 applies the models to five HRI observations and § 5 presents the conclusions.

2. METHOD

The calibration of the particle background of the HRI is considerably more problematic than that for the PSPC (Snowden et al. 1992; Plucinsky et al. 1993). While the PSPC had an internal mechanism for measuring the total PB count rate, the HRI has no useful secondary monitor (the HRI "invalid" count rate comes close but has poor statistics combined with additional nonstatistical scatter). Thus, an estimate for the HRI PB must be derived from other available quantities. This difficulty is compounded by the intrinsically high HRI PB rate, which requires one to subtract a large value (the model PB counts) from another similarly large value (the total observed counts) to result in a much smaller residual, which is the cosmic signal.

2.1. The PSPC Master Veto

The *ROSAT* PSPC was equipped with electronics to provide five-sided vetoing. In essence, it was possible to separate events originating in the active region behind the entrance window of the proportional counter from those associated with simultaneous events occurring at the back and along the sides of the detector (which because of the detector geometry had to be produced by cosmic rays). This eliminates most PB events as they leave tracks of charge running through the detector. In addition, screening electronics were able to identify additional non-cosmic events by their deposited charge distributions (Metzner 1986). Together, occurrences of all the events identified as being non-cosmic in origin by the detector were linked in a signal called the master veto (MV), which was used in anticoincidence with the total signal to identify "good" events.

The MV count rate (MV) was telemetered to ground and was incorporated in a useful form in observation data products. With further processing it became apparent that MV was a relatively stable function of the geographic subsatellite point (e.g., Snowden et al. 1992). This stability was enhanced by the nearly circular *ROSAT* orbit which effectively eliminated the dependence of the particle background on altitude. While the altitude of the satellite does vary because of the oblateness of the Earth, it is nearly constant for repeated passages over the same geographic location. Intrinsic variations of the particle background and any variation caused by the slow decay of the *ROSAT* orbit were smoothed and averaged out by the extensive multiple coverage. Figure 1a displays a map of MV in geographic coordinates. Because of the count-rate limitations, the PSPC was only able to operate at lower geomagnetic latitudes than the particle belts and away from the South Atlantic Anomaly (SAA). MV increases from a minimum of ~ 50 counts s^{-1} at the geomagnetic equator to ~ 250 counts s^{-1} near the belts.

2.2. The HRI Primary Count Rate and PSPC MV

Besides information on individual events, several counters are available in standard processed HRI data. One of these counters is the primary count rate (PCR) which reports the number of accepted and telemetered events. To examine the relation between the PCR and MV, however, is not directly possible since the PSPC and HRI were never operated simultaneously in scientific mode. To circumvent this limitation, and to eventually produce a useful calibration, PCR is compared to the average MV rate (given by the data in Fig. 1a) as a function of geographic subsatellite position.

To perform this correlation, the TREND data set (Reichert & Snowden 1994) is used. TREND data have been produced by the U. S. *ROSAT* Science Data Center (USRSDC) Guest Observer Facility at Goddard Space Flight Center (GSFC) to allow a convenient method for examining the satellite and instrument status on a daily basis. TREND files each consist of one *ROSAT* day worth of data (*ROSAT* days are defined by the ground station contact cycle and are typically slightly less than one standard day due to precession of the satellite orbit). There are entries for each 60 s interval with geometric (e.g., satellite position and pointing direction), science (e.g., PCR and MV), and instrument and satellite status (e.g., temperature and voltage monitors) information.

The first step in the calibration process is to make scatter plots of the PCR versus MV. For each 60 s interval when the HRI is operating, the PCR and geographic longitude and latitude are read from the TREND file. Using the geographic longitude and latitude, the average MV count rate is determined from the MV map. Data from typically about one month are collected for an individual plot and correlation. Figure 2 shows two examples of such plots using data collected in 1991 February and March and 1994 June.

The structure in Figure 2 requires some explanation. The general diagonal trend of the data indicates a correlation of PCR with MV, and thus implies a correlation with cosmic-ray intensity. Most of the data lie along the lower trajectory in each plot but both have two additional parallel trajectories higher in the plots. The reason for this type of distribution is that while most observations have no strong cosmic sources in the field of view and the count rate is dominated by the PB, when relatively bright sources are observed (greater than a couple counts per second) obvious vertical shifts in the distribution are produced. In the case of the two high trajectories in Figure 2a, the sources have count rates of $\sim$ 5.5 counts s^{-1} and $\sim$ 11.5 counts s^{-1} while in Figure 2b, the sources have count rates of $\sim$ 5 counts s^{-1} and $\sim$ 12 counts s^{-1}. That most of the points lie in the lower trajectories indicates that, in general, point sources and the cosmic diffuse background do not contribute extensively to the overall count rate. The slight turn-up for $MV \gtrsim 175$ counts s^{-1} in Figure 2b will be discussed in § 2.4.

It is important to note that the lower trajectory can be extrapolated back to zero MV with a count rate consistent with what is expected from the "typical" cosmic background ($\sim$ 1 count s^{-1}, David et al. 1997). This implies that any noncosmic background intrinsic to the HRI (e.g., residual radioactivity in the glass or any other "dark current") is a minor contributor to the total background ($\lesssim$ 0.5 counts s^{-1} compared to a minimum of $\sim$ 2.5 counts s^{-1} for the PB) and that, by extension, microchannel plates similar to the HRI are sensitive to cosmic rays, producing an intense background in low Earth orbit.

2.3. Temporal Calibration of the HRI Particle Background

The relation between PCR and MV exhibited in Figure 2 provides a mechanism for a practical calibration the HRI particle background. The lower trajectories provide the required relation, albeit with considerable scatter (typical statistical errors are $\sim$ 0.3 counts s^{-1}). With the assumption that the data along the trajectories are randomly sampling the sky (and therefore provide an unbiased sample of the average cosmic signal), linear fits to the data (shown by the dashed lines in Fig. 2) after excluding the upper trajectories provide the scale factors (slopes of the trajectories) between MV and the HRI PCR (for the different time intervals), but the offsets (PCR value when the trajectory is extrapolated back to $MV = 0$) include cosmic X-rays and any additional constant contamination (e.g., dark current). With the further assumption that the offsets are dominated by cosmic X-rays, an estimate of the typical contribution ($\sim$ 0.75 counts s^{-1}) of the cosmic X-ray background to the HRI count rate can be subtracted to provide the final relations (the solid lines in Fig. 2). This is an admittedly messy way to go about calibrating the PB as it is only able to provide an estimate for the average background at any given time. Inherent in this calibration is the assumption that the minimum PB count rate scales with the minimum MV count rate. That is, that the HRI count rate increasing from $\sim$ 3.0 to $\sim$ 5.0 counts s^{-1} as MV goes from $\sim$ 50 to $\sim$ 100 counts s^{-1} implies that the HRI PB rate at $MV \sim 50$ counts s^{-1} is $\sim$ 2.0 counts s^{-1}.

There are two additional significant complications to the calibration. The first arises from the eventual desire to apply pulse-height and detector-area restrictions to the accepted data (discussed below in § 3). The second complication arises from the fact that the correlation between *PCR* and a single average *MV* map is not constant with time. The flux of cosmic rays experienced by *ROSAT* in its low-Earth orbit is lower during solar maximum and higher during the intermaximum period consistent with predictions (Stassinopoulos, Barth, & Smith 1989). This effect is illustrated in the two plots in Figure 2 where the data in the upper panel are from early 1991 and the data in the lower panel are from mid 1994. The slope of the lower trajectory in Figure 2a is ~ 0.042 (*PCR* counts s^{-1})(*MV* counts s^{-1})$^{-1}$ compared to ~ 0.052 (*PCR* counts s^{-1})(*MV* counts s^{-1})$^{-1}$ for the lower trajectory in Figure 2b. The trend of this effect over the life of the mission can be seen in the fitted values for the scale factor (slope) between the *MV* map and the HRI *PCR* shown in Figure 3, which increase from launch (near solar maximum) to a plateau starting in mid 1993 (well away from the solar maximum). Table 1 lists the fitted values of the scale factor and offset for the mission thus far (1997 Fall). Note that this variation of the slope is due to the limitation of comparing the *PCR* data to the average *MV* map. If it were possible to compare simultaneous *MV* and *PCR* data throughout the mission it is likely that the scaling would be constant, i.e., that both the *MV* and *PCR* scale in a similar manner with the variation of the particle background during the solar cycle.

On a side note, while the scatter in Figure 3 is at the $\pm 10\%$ level, the fitted scale factor is strongly correlated with the fitted offset (Fig. 4) suggesting that the true variation could be less. In this case a larger scale factor is compensated by a smaller offset producing a line in the dynamic range where there are data with greater consistency than suggested by the values for the scale factor alone. To illustrate this further, the data were refit fixing the offset value at 0.75 counts s^{-1} (a typical value from Fig. 4). While the data from launch until early 1993 (spacecraft, S/C, clock $\sim 8 \times 10^7$ s) typically required a larger offset and so the fits with the fixed offset were not as good (by visual examination), the data from later in the mission were typically well fit. Figure 5 plots the fitted scale factors when the offset is fixed and shows considerably lower scatter than Figure 3, suggesting relatively little short-term (on the order of months) temporal variation after the plateau was reached. However, the fitted offsets (minus the 0.75 counts s^{-1} attributed to the cosmic background) and scale factors are used for the calibration.

2.4. Another Minor Complication

While the use of the *MV* map as a template for the HRI PB works well for observations through 1995, as the mission has progressed more of the orbit has been used for observations. In particular, some data during passages of the particle belts as well as those from deeper passages into the SAA have been included. In order to estimate the PB in the region of extended orbital coverage (beyond that sampled by the PSPC), the HRI count rate in channels $2-10$ (the selected channel range is discussed below in § 3) within a detector radius of $17\farcm5$ from observations with only faint sources ($\lesssim 1$ count s^{-1} cosmic contribution) were cast into geographic coordinates. This processing included $\sim 10.3 \times 10^6$ s of data from 298 observations. The resultant count-rate image was compared to the MV map of Figure 1a and an offset and scale factor were fit over the ranges $MV < 150$ counts s^{-1} and HRI count rate of < 5 counts s^{-1}. The data and fit are shown in a scatter plot in Figure 6. The data are tightly correlated in the range $MV < 150$ counts s^{-1}, while out of that range the HRI count rate is relatively higher than MV. This same effect can be seen in Figure 2b (it is more obscure in Fig. 2a). In addition, it is interesting to note that the divergence begins at roughly the same MV rate as that for the PSPC PB as shown in Snowden et al. (1992) Figure 8. This effect suggests a difference in the responses of the different technology detectors to a changing population of cosmic rays as the satellite approaches the particle belts and SAA. In order to use the temporal calibration of § 2.3, the fitted offset and linear scale factor are used to scale the HRI count rate image to an effective MV map, which is shown in Figure 1b. The fit can be extrapolated back to an HRI count rate of 0.93 counts s^{-1} at $MV = 0$ counts s^{-1}, reasonably consistent with the count rate expected from cosmic X-rays. The MV map is used in determining the basic calibration (i.e., the data in Table 1) while the HRI-derived map is used to model the light curves of individual observations.

2.5. Alternative Measures

For perhaps academic interest there are alternative, if not as satisfactory, samples which can be used to estimate the HRI PB. Perhaps any measure of the cosmic-ray flux at the satellite's altitude which has mapped the geographic regions where the HRI is active can be substituted for the MV. The South Atlantic Anomaly Detector (SAAD, Pfeffermann et al. 1987) on board *ROSAT* is one, the geomagnetic MacIlwain L parameter is another.

The SAAD is a solid state (10 cm^2 germanium) detector which was flown to provide a backup mechanism for protecting the PSPC from damage due to high PB rates. The average SAAD rate (see Fig. 1, Snowden et al. 1992) correlates well with the average MV rate (Fig. 7) except for regions near the SAA where the SAAD is relatively higher and near the particle belts where it is relatively lower. The SAAD would have provided the most logical measure of the PB as it is in operation simultaneously with the HRI, however the necessary data product was not included in the HRI reduction stream in the Standard Analysis Software System (SASS, Gruber 1992; Voges et al. 1992). Never-the-less, using an average SAAD map for the modeling provides fits to the data comparable to, to slightly worse than, the MV modeling. Figure 8 shows a scatter plot comparing SAAD and HRI data.

The geomagnetic MacIlwain L parameter provides another, less accurate measure, but it has the advantage of being defined over the entire globe for a wide range of altitudes. However, it may not be useful poleward from the particle belts nor does it reflect the SAA. Modeling code for magnetic field parameters such as the MacIlwain L value can be obtained from the National Space Science Data Center (NSSDC). Figure 9 displays the correlation in a scatter plot of the MV versus the L value. The main reason for the scatter outside of the tightly correlated points (middle trajectory) is that the L value does not reflect the SAA (the lower trajectory) and is relatively larger near the particle belts (upper trajectory).

3. PARTICLE BACKGROUND AND QUANTUM EFFICIENCY DETECTOR MAPS

The creation of detector maps for the particle background and quantum efficiency (including vignetting) is problematic. It is ideal to create the maps from flight data to accurately reflect the operational geometries and orbital environment. Unfortunately, true cosmic flat fields are difficult to come by. However, there is a data product produced by the SASS processing which can be used. These are the Earth block data files which contain events that are collected while Earth is in the observation field of view. Thus, they contain data both when the Sun-lit or "bright Earth" as well as the night-side or "dark Earth" are in the field. The bright-Earth data, which are dominated by scattered solar X-rays and in particular the oxygen Kα emission line at 525 eV (Snowden & Freyberg 1993), provide an effective flat field for the vignetting and quantum efficiency detector map to be used in exposure correction. The limitation here is that the X-ray Telescope (XRT, Aschenbach 1988) vignetting is energy dependent (it is more severe at higher energies) so the detector map will not be as appropriate for sources with particularly hard spectra. The dark-Earth data provide exposure time dominated by the PB and thus provide a PB detector map.

The TREND data are again used in this analysis. The zenith angle (Z) TREND entry is used to select observation intervals where the observation line of sight is completely blocked by Earth ($Z > 115°$). The Sun-Earth-satellite angle (SES), geographic position, and primary count rate (PCR) TREND entries are used to separate bright-Earth from dark-Earth data. If $SES < 100°$, the data are considered to be bright Earth. The geographic position is used to predict the expected PB rate using the temporal calibration of the preceeding section, and the prediction is then compared to the PCR TREND entry. If $100° < SES < 110°$ and the PCR is greater than the model PB prediction plus 3 counts s^{-1}, the data are considered to be bright Earth. This ambiguity near the terminator is caused by the varying observation geometry as, depending on the pointing direction in sky coordinates, the HRI could be looking either toward the sunlit or dark Earth. If $SES > 100°$ and the PCR is less than the model PB prediction plus 1.5 counts s^{-1}, the data are considered to be dark Earth. If $SES > 110°$, the data are considered to be dark Earth.

All of the available Earth block data files have been processed creating a dark-Earth map with 6.47×10^5 counts. This is an insufficient number of counts to be useful with a $5'' \times 5''$ pixel size ($\sim$ 4 counts per pixel) so the data were smoothed over $30'' \times 30''$ regions. A bright-Earth map with 2.76×10^7 counts was created with a PB model prediction of 3.13×10^6 counts. The dark-Earth map was used to subtract the model PB counts from the bright-Earth map. Finally, a flattening (the average of the data and a flat distribution was used) and slight tilting (a gradient of $\sim 2\%$) of the PB detector map was empirically required to insure that flat fields were indeed flat. These corrections were determined from deep exposures of regions without structure in the cosmic background. At least some of the requirement for this "fudge" likely arises from the residual contribution of atmospheric X-rays (vignetted) acquired during times when the satellite was near the terminator.

Two additional selection criteria were applied to the data. First, events with pulse-heights outside of the range $2 - 10$ were excluded. Cosmic X-ray events are primarily detected with pulse heights in this range and so by excluding the events in observation data reduction, the signal (cosmic X-rays) to noise (cosmic-ray events) ratio can be significantly improved. Note that this is the same channel range used in creating the effective MV map. This consistency in the use of the specified channel range avoids any complications if the distribution of PB events on the detector is channel dependent. Second, data outside of a $\sim 17\rlap{.}'5$ radius were excluded to remove detector-edge effects.

4. APPLICATION OF THE RESULTS

To apply the particle background calibration to a given observation, a simple linear interpolation of the fitted parameters of § 2.3 to the appropriate times and the satellite geographic coordinates is first used to produce a model PB light curve, $R_{mod}[t]$, the model count rate as a function of time. To increase the accuracy of the model for a specific observation, $R_{mod}(t)$ is fit to the observation light curve, $R_{obs}[t]$, the observed count rate over the selected region of the detector in the selected channel range as a function of time, using a linear relation ($R_{obs}[t] = \alpha + \beta \times R_{mod}[t]$) where the fitted parameter β provides the final scaling and α represents the cosmic diffuse background, point sources, and any additional constant contamination. The final scaling is required anyway by the use of the restricted pulse-height range and detector area noted in § 3. (These restrictions are not applied in the production of the PCR in the TREND data.)

It should be noted that longer observations which include more samples at various geographic positions will have more accurate estimates due to a smaller probability of sampling only regions where there are significant systematic errors in the MV to PCR calibration. A bright point source in an observation should not affect the results excessively as long as any variations in the source count rate have periods much shorter than the observation length. They can, however, greatly increase the χ^2_ν value of the fit. This is particularly true when even a constant bright source is near the edge of the field and is periodically wobbled off the detector.

The Extended Source Analysis Software (ESAS) package of Snowden (1995) contains the programs CAST_DATA_HRI and CAST_EXPPAR_HRI. CAST_DATA_HRI casts the detected events in pulse-height channels $2 - 10$ with selection radii of $8'$, $12\rlap{.}'5$, or $17\rlap{.}'5$ into sky coordinates and produces an observation light curve. CAST_EXPPAR_HRI models the HRI PB (including a final fitting of the model to the observation light curve) and the effective exposure and casts them into sky coordinates (with the same radius selection). In this section, the modeling and software

are applied to five HRI observations. The first four, M101, IC 2391, a region of the SMC, and NGC 6822 are distributed throughout the mission and have relatively small cosmic contributions. The fifth is of a bright portion of the Cygnus Loop supernova remnant (SNR). See Table 2 for details of the observations.

4.1. M101

Figure 10 shows the fitted light curve for the M101 observation produced by CAST_DATA_HRI and CAST_EXPPAR_HRI. The curve shows the model prediction for the PB after the final scaling of the calibration, which indicated a decrease of 52% from the initial values (dominated by the pulse-height range and radius restrictions). While there is some structure in the residuals, there are no general trends. The constant component which includes the cosmic background, point sources, and any additional contamination component is 0.75 counts s^{-1}. The fit to the data yielded a χ^2_ν value of 1.06 with 1362 degrees of freedom. Details of the data reduction can be found in Table 3.

The next set of figures shows the effect of the PB on the image of M101. Figure 11a shows the smoothed count image produced by CAST_DATA_HRI. There are 106527 counts in the image. From the original data set, 32875 events were excluded by the pulse-height selection and 22803 were excluded by the radius selection. Of the remaining counts, 86592 are modeled as PB by CAST_EXPPAR_HRI (implying that $\lesssim$ 19% of the final counts are cosmic in origin). The counts are relatively flat as they are dominated by the PB and point sources have been masked out. There is, however, an enhancement in the count density in the center of the field consistent with emission from M101.

Figure 11b displays the exposure-corrected image of M101 where the count map has been divided by the exposure map. Notice that while there is still a slight enhancement near the center of the image consistent with emission from M101, there is also an enhancement around the edge of the field. This is due to “incorrectly” correcting the flat particle background with the vignetted exposure map. Figure 11c shows the background-subtracted and exposure-corrected M101 image where the model background count map is subtracted from the observed count map and the result is divided by the exposure map. The enhancement due to emission from M101 is considerably clearer while the rest of the field appears relatively flat.

Another way of considering the differences produced by exposure correction and background subtraction is to examine the radial profiles of the images. Figure 12a shows the radial profile of the original count image with point sources masked (the radial profile of Fig. 11a). The profile is slightly peaked at the center of the image again implying the existence of additional emission from M101. This is consistent with the PSPC results of Snowden & Pietsch (1995) which showed extensive diffuse emission from the galaxy. The fall-off of count density beyond $17'$ is due to the satellite wobble causing a large variation in the effective exposure at the edges of the field.

Figure 12b shows the surface brightness radial profile of the exposure-corrected count image after masking of point sources (the radial profile of Fig. 11b). The excess at the center is still present but now there is a marked enhancement for angles greater than $10'$. Again, this is an artifact of applying the vignetting correction to the relatively flat PB, and clearly demonstrates the necessity of a PB subtraction. Figure 12c shows the surface brightness radial profile of the M101 image after background subtraction and exposure correction (the radial profile of Fig. 11c). The enhancement at the center of the field is clear and consistent with the PSPC results. Converting the PSPC surface brightness away from M101 measured by Snowden & Pietsch (1995), $\sim 2 \times 10^{-3}$ counts s^{-1} arcmin^{-2}, to an HRI surface brightness produces an expected intensity of $\sim 5 \times 10^{-4}$ counts s^{-1} arcmin^{-2}. This is consistent with the profile of Figure 12c indicating that the reduction is reasonably correct.

4.2. IC 2391

The second test observation is of IC 2391. This was a particularly long (55 ks) observation with individual observation intervals spread over two months. The χ^2_ν of the fit at 1.19 is somewhat worse than that for M101 (1.06) but certainly still acceptable in a practical if not formally statistical sense. Again, the results of the data reduction are listed in Table 3. The count profile, exposure-corrected surface brightness profile, and exposure-corrected and background-subtracted surface brightness profile are shown in Figure 13.

As for the M101 radial profile away from M101 emission, the exposure-corrected and background-subtracted distribution for the IC 2391 image appears relatively flat with an average surface brightness consistent with the cosmic background.

4.3. SMC #2

The third test observation is one of the survey observations of the SMC, SMC #2. This observation was done in early 1997 and includes a significant additional sample of the orbital environment in the southern hemisphere including passages though the particle belts and incursions into the SAA. The χ^2_ν of the fit at 1.57 is significantly worse than those for M101 (1.06) and IC 2391 (1.19). The increase in χ^2_ν has two major contributors. The first and largest is a 301 s interval where the model greatly underpredicts the data. Removing this atypical interval ($\sim 1\%$ of the data) by examining the model fit to the light curve reduces the χ^2_ν value to 1.32. The second contributor to the large χ^2_ν value is a general poorness of fit at high values of MV, a systematic underprediction by the model. This is likely due to a reduced ability to model the PB within the particle belts and SAA because of a lack in the consistency of background rates during different observations. This effect may be reduced as more data are incorporated into the effective MV map.

Table 3 lists the results of the data reduction for both the full data set and after exclusion of the atypical 301 s interval. The count profile, exposure-corrected count rate profile, and exposure-corrected and background-subtracted count rate profile are shown in Figure 14. The final background-subtracted and exposure-corrected profile (Fig. 14c) in this case is not flat, although as expected it is flatter than the profile in Figure 14b. The edge enhancement is reduced from $\sim 1 \times 10^{-3}$ counts s^{-1} arcmin^{-2} to $\sim 0.5 \times 10^{-3}$ counts s^{-1} arcmin^{-2}. Most of the residual off-axis increase in Figure 14c is due to an enhancement on one side of the image. Figure 15 shows a heavily smoothed, background-subtracted, and exposure-corrected image of the observation. Note the enhancement along the right-hand rim of the field. Figure 16 shows a horizontal cut across the field. At this point it is not clear what causes this enhancement, although a PSPC observation of the same region rules out a significant cosmic contribution. A possible explanation is a changing distribution with time of background counts across the detector (however, see the following section). The excess counts are not associated with the increased sampling of the particle belts and SAA as the gradient is still seen after excluding those regions. While this may be a pathological case of an enhanced noncosmic background component affecting just this one observation, the final background-subtracted and exposure-corrected images for all observations should be examined for such effects.

4.4. NGC 6822

The fourth test observation is of NGC 6822, an irregular galaxy in the local group. This observation was done in 1996 October and also includes a sampling of the northern and southern particle belts. The χ^2_ν of the fit at 1.26 is again worse than those for M101 (1.06) and IC 2391 (1.19), although it is better than that for SMC #2 (1.57). However, the χ^2_ν value does agree well with that for the SMC #2 observation after its atypical 301 s interval was removed from the analysis (1.32). As with the SMC #2 observation, the relatively high χ^2_ν value is due to a systematic underprediction of the light curve at the largest values, those associated with passages through the particle belts.

Again, the results of the data reduction are listed in Table 3. The count profile, exposure-corrected count rate profile, and exposure-corrected and background-subtracted count rate profile are shown in Figure 17. Unlike the SMC observation, the final background-subtracted and exposure-corrected profile (Fig. 17c) is again flat. The edge enhancement apparent in the SMC (Fig. 14c) is not reproduced in the NGC 6822 observation suggesting that the enhancement is not a general feature of later observations.

4.5. Cygnus Loop

Figure 18 shows the light curve for the Cygnus Loop observation. As for the M101 light curve, the line shows the model prediction for the PB after the final scaling of the calibration. The Cygnus Loop is very bright, even when observed by the HRI. The final fitted offset implies a count rate of ~ 28 counts s^{-1}. The considerable ripple in the light curve ($\sim \pm 4$ counts s^{-1} around the PB model curve) shows the effect of part of the SNR being wobbled in and out of the field of view. The final fitting of the PB scale factor indicated a decrease of 62% from the initial values (compared to 52% for the M101 observation). The larger fitted value for the decrease is likely due to the confusion caused by the large amount of ripple. The χ^2_ν value for the fit is 2.94 with 1070 degrees of freedom. The structure in the residuals reflects the ripple in the light curve but little else.

Figures 11d,e,f show the same set of images for the Cygnus Loop observation as Figures 11a,b,c do for M101. There are 697564 events in the count image and there were 76169 events excluded by the pulse-height selection and 82432 events excluded by the radius selection. Of the remaining counts, 38562 are modeled as PB. Again, the results of the data reduction are listed in Table 3.

Figure 19 shows the counts, exposure-corrected count rate, and background-subtracted and exposure-corrected count rate for a horizontal cut across the center of the image. The cut clearly shows the necessity for exposure correction (including quantum-efficiency effects) at the right-hand end of the cut. The count image falls off by $\sim 12\%$ more between the center and $16'$ (just before the drop due to the wobble) than the exposure-corrected image. For an object as bright as the Cygnus Loop, the PB subtraction has a less obvious impact.

5. CONCLUSIONS

The particle background of the *ROSAT* HRI has been analyzed and a model calibration presented with practical applications to the observations of the face-on galaxy M101, IC 2391, a region of the SMC, NGC 6822, and a region of the Cygnus Loop supernova remnant. The satellite position as a function of time is compared to a map derived from the HRI count rate from selected observations with small cosmic contributions which has been scaled to a map of the *ROSAT* PSPC master veto. The model light curve is fit to the observation light curve for a final scaling.

It is found that this general temporal model coupled to the final scaling well fits observation light curves with typical values of $\chi^2_\nu \sim 1 - 1.5$ with two free parameters for non-pathological cases (e.g., Cygnus Loop), although bright point sources can increase the χ^2_ν value significantly (e.g., $\chi^2_\nu \sim 6$ for an observation with the bright LMC SNR N132D on the edge of the observation field).

This modeling can likely be extended to any cosmic-ray sensitive detector in low-Earth orbit. Specifically, the tight correlations between the PSPC (proportional counter), HRI (microchannel plate), and SAAD (solid state) detectors show this for three distinctly different detector technologies.

The software used in this paper (CAST_DATA_HRI and CAST_EXPPAR_HRI) can be found in the USRSDC area in the High Energy Astrophysics Science Archive (HEASARC) Legacy anonymous ftp site at GSFC (ftp legacy.gsfc.nasa.gov, cd rosat/software/fortran/sxrb).

I would like to thank D. Harris and K. Kuntz for a number of useful suggestions which improved the clarity of this paper.

REFERENCES

Aschenbach, B. 1988, Appl. Opt., 27, No. 8, 1404

David, L. P., et al. 1997, The *ROSAT* High Resolution Imager (HRI) Calibration Report, 1997 Revision, (USRSDC, SAO)

Fraser, G. W. 1989, X-ray Detectors in Astronomy, (Cambridge:Cambridge University Press), pp 116

Gruber, R. 1992, in Data Analysis in Astronomy IV, ed. V. Di Gesù et al. (New York:Plenum), 153

Henry, P., & Henriksen, M. J. 1986, ApJ, 301, 689

Henry, P., Kellogg, E., Briel, U. G., Murray, S., van Speybroeck, L., & Bjorkholm, P. 1977, Proc. SPIE, 106, 196

Kellogg, E., Henry, P., Murray, S., van Speybroeck, L., & Bjorkholm, P. 1976, Rev. Sci. Instr., 47, 282

Metzner, G. 1986, Nucl. Instr. Methods, A242, 493

Pfeffermann, E., et al. 1987, Proc. SPIE, 733, 519

Plucinsky, P. P., Snowden, S. L., Briel, U. G, Hasinger, G., & Pfeffermann, E. 1993, ApJ, 418, 519

Reichert, G., & Snowden, S. L. 1994, A Guide to ROSAT TREND Data, NASA/GSFC, USRSDC

Snowden, S. L. 1995, Cookbook for Analysis Procedures for *ROSAT* XRT/PSPC Observations of Extended Objects and the Diffuse Background, NASA/GSFC, USRSDC

Snowden, S. L., & Freyberg, M. J. 1993, ApJ, 404, 403

Snowden, S. L., McCammon, D., Burrows, D. N., & Mendenhall, J. A. 1994b, ApJ, 424, 714

Snowden, S. L., & Pietsch, W. 1995, ApJ, 452, 627

Snowden, S. L., Plucinsky, P. P., Briel, U., Hasinger, G., & Pfeffermann, E. 1992, ApJ, 393, 81

Stassinopoulos, E. G., Barth, J. M., & Smith, R. L. 1989, NAE Charged Particle Environment Study (NASA:GSFC)

Trümper, J. 1983, Adv. Space Res., 2(4), 241

Trümper, J. 1992, QJRAS, 33, 165

Voges, W. et al. 1992, in Proceedings of Satellite Symposium 3, Space Science with particular emphasis on High-Energy Astrophysics, ed. T. D. Guyenne & J. J. Hunt (Noordwijk:ESA Publications Division), 223

Zombeck, M. V., David, L. P., Harnden, Jr., F. R., and Kearns, K. 1995, Proc. SPIE, Vol. 2518, 304

This preprint was prepared with the AAS LaTeX macros v4.0.

Fig. 1.— a) Map in geographic coordinates of the PSPC master veto count rate (MV). The map was created from TREND data and has been smoothed for presentation and PB modeling. The large region of missing data in the south outlines the South Atlantic Anomaly (SAA) where the PSPC was switched off to protect it from high PB rates. The smaller regions of missing data in both the north and south outline the regions of the *ROSAT* orbit affected by Earth's particle belts. b) Map in geographic coordinates of the HRI count rate in channels $2-10$ scaled to the MV rate (see text). The grey scales range from 50 to 300 counts s^{-1} with contours at 60, 75, 100, 150, and 250 counts s^{-1}.

Fig. 2.— Scatter plot of the HRI primary count rate (PCR) versus average PSPC master veto count rate (MV) from a) 1991 February - March and b) 1994 June. Units are counts s^{-1}. The dashed lines show the fitted correlation of the lower trajectories. The solid lines show the estimate for the HRI particle background (the fitted lines minus 0.75 count s^{-1}). Typical errors are $\sim$ 0.3 counts s^{-1}.

Fig. 3.— Scatter plot of the fitted value for the scale factor between the HRI PCR and PSPC master veto (MV) as a function of spacecraft (S/C) clock seconds (S/C clock is zero at *ROSAT* launch, 1990 June 1, 21:06:50 UT). The units for the scale factor are (PCR counts s^{-1}) (MV counts s^{-1})$^{-1}$.

Fig. 4.— Scatter plot of the fitted value for the scale factor between the PCR and MV versus the fitted value of the offset. Only data with S/C clock times greater than 10^8 s were used. The units for the scale factor are (PCR counts s^{-1}) (MV counts s^{-1})$^{-1}$.

Fig. 5.— Scatter plot of the fitted value for the scale factor between the PCR and MV as a function of S/C clock when the offset is fixed at 0.75 counts s^{-1}. The units for the scale factor are (PCR counts s^{-1}) (MV counts s^{-1})$^{-1}$.

Fig. 6.— Scatter plot comparing the average MV count rate (the data in Fig. 1a) to the average HRI count rate in the channel range $2-10$ within a detector radius of $17\overset{\prime}{.}5$ (the data used in Fig. 1b before they were scaled). The line shows the best-fit linear relation for data with $MV < 150$ counts s^{-1} and HRI count rate < 5 counts s^{-1}.

Fig. 7.— Scatter plot comparing the average MV count rate (the data in Fig. 1a) to the average *ROSAT* South Atlantic Anomaly Detector (SAAD) count rate (the SAAD data were cast into a map similar to that for the MV data fin Fig. 1a and can be seen in Fig.1 of Snowden et al. 1992).

Fig. 8.— Scatter plot comparing the average SAAD rate to the average HRI count rate in the channel range $2-10$ within a detector radius of $17\overset{\prime}{.}5$ (the data in Fig. 1b before they were scaled).

Fig. 9.— Scatter plot comparing the average MV count rate (the data in Fig. 1a) to the average MacIlwain L parameter (L value).

Fig. 10.— Light curve (upper panel in counts s^{-1}) and fit residuals (lower panel in sigmas) of the

M101 observation. The data in channels $2-10$ within a radius of $17\rlap{.}'5$ have been binned to provide an average count rate in 20 s intervals. The model curve, mostly obscured by the data points, includes a fitted final scaling of the model prediction.

Fig. 11.— Images of the M101 and Cygnus Loop observations. The data have been binned into $20'' \times 20''$ pixels and have been smoothed after the removal of point sources (white spots). a) M101 count image with a linear scaling between 0 and 140 counts arcmin^{-2} with contours at 25, 50, 75, 100, and 125 counts arcmin^{-2}. b) M101 exposure-corrected image (count image divided by the exposure map) with a linear scaling over the range $(2.5-4.5) \times 10^{-3}$ counts s^{-1} arcmin^{-2} with contours at 3.0, 3.5, 4.0, and 4.5×10^{-3} counts s^{-1} arcmin^{-2}. c) M101 particle background-subtracted and exposure-corrected image (count image minus the PB map which is then divided by the exposure map) with a linear scaling between 0 and 1.25×10^{-3} counts s^{-1} arcmin^{-2} with contours at at 0.25, 0.5, 0.75, and 1.0×10^{-3} counts s^{-1} arcmin^{-2}. The excess in the inner $\sim 7'$ is due to emission from M101. d) Cygnus Loop count image with a square-root scaling between 0 and 4000 counts arcmin^{-2} with contours at 50, 100, 250, 500, 1000, 1500, 2000, and 2500 counts arcmin^{-2}. e) Cygnus Loop exposure-corrected image with a square-root scaling between 0 and 0.18 counts s^{-1} arcmin^{-2} with contours at 3.5, 5.0, 10.0, 25.0, 50.0, 75.0, 100.0, and 125.0×10^{-3} counts s^{-1} arcmin^{-2}. f) Cygnus Loop background-subtracted and exposure-corrected image with the same scaling as e) but with contours at 1.5, 2.5, 5.0, 10.0, 25.0, 50.0, 75.0, 100.0, and 125.0×10^{-3} counts s^{-1} arcmin^{-2}. Note the difference in apparent small-scale structure of the remnant at the edge of the field when comparing the corrected image and the original count image.

Fig. 12.— Radial profiles of the M101 observation. a) Count density in units of counts arcmin^{-2}. Data are binned in $30''$ annuli. b) Exposure corrected profile. c) Background-subtracted and exposure-corrected profile. For Figs. b,c the data are binned in $1'$ annuli and the units are counts s^{-1} arcmin^{-2}. Point sources have been masked for all profiles. The central excess is due to emission from M101.

Fig. 13.— Radial profiles of the IC 2391 observation. The panels are the same as for Fig. 12.

Fig. 14.— Radial profiles of the SMC #2 observation. The panels are the same as for Fig. 12.

Fig. 15.— Grey scale image of the SMC #2 observation. The data have been particle background-subtracted and exposure-corrected (count image minus the PB map which is then divided by the exposure map) with a linear scaling between 0.45 and 1.40×10^{-3} counts s^{-1} arcmin^{-2} with contours at at 0.5, 0.75, 1.0, and 1.25×10^{-3} counts s^{-1} arcmin^{-2}. The data have been heavily smoothed to enhance the visibility of the edge enhancement (visible along the right-hand side) discussed in the text.

Fig. 16.— A horizontal cut through the background-subtracted and exposure-corrected SMC #2 observation. Units are counts s^{-1} arcmin^{-2}.

Fig. 17.— Radial profiles of the NGC 6822 observation. The panels are the same as for Fig. 12.

Fig. 18.— Light curve (upper panel) and fit residuals (lower panel) of the Cygnus Loop observation. The model curve includes a fitted final scaling of the model prediction. Note the ripple of the data around the model line due to bright parts of the Cygnus Loop being wobbled in and out of the field of view. The units, data selection, and binning are the same as for the M101 data in Fig. 10.

Fig. 19.— Horizontal cuts across the Cygnus Loop observation. a) Count density in units of counts arcmin^{-2}. Data are binned in $40''$ steps. b) Exposure-corrected profile in units of counts s^{-1} arcmin^{-2}. c) Background-subtracted and exposure-corrected profile in units of counts s^{-1} arcmin^{-2}. Note that the off-Loop data are relatively flat but that the intensity of the residual signal is significantly higher than for the other observations. The excess is due to the smaller fitted scaling of the PB model caused by confusion of the wobble-induced ripple.

Table 1. Time intervals and fitted scale factors and offsets for analysis.

Start Time[a]	End Time[a]	Scale Factor[b]	Offset[c]
2372890	5022010	0.03402	1.580
21867370	25609870	0.04180	1.553
28331830	29183410	0.04672	1.276
38973430	42290290	0.04293	1.190
44164330	45439930	0.04474	1.427
47738470	50972830	0.04613	1.143
56163970	57013510	0.04495	1.251
59315290	63911830	0.04619	1.187
65099470	68587930	0.05194	0.720
71996050	75908410	0.04868	1.318
78122590	80081590	0.04957	1.026
83227090	86037070	0.05629	0.507
88078510	91146130	0.05227	1.099
93015130	95824330	0.04883	1.176
112247590	114401890	0.05387	0.856
115851970	118036450	0.05338	0.855
118460590	120672730	0.05741	0.242
121102750	123394870	0.05178	0.856
123910870	126122890	0.05508	0.571
126632950	128672890	0.05198	0.875
129268930	131508730	0.05202	0.857
131508730	134144710	0.04984	0.912
134144770	136700470	0.05450	0.680
136700530	139422370	0.05285	0.832
139422430	141978010	0.05299	0.992
141978010	144699730	0.05473	0.500
144699790	147341170	0.05322	0.671
147341230	149805010	0.05383	0.652
149805010	152446330	0.05447	0.655
152446390	155081890	0.05468	0.693
155081950	157723150	0.05276	0.785
157723210	160358650	0.05100	0.907
160358650	162999790	0.05303	0.748
162999850	165721150	0.05455	0.724

Table 1—Continued

Start Time[a]	End Time[a]	Scale Factor[b]	Offset[c]
165721210	168276370	0.05345	0.726
168276430	170911690	0.05640	0.581
170911750	173552710	0.05417	0.649
173552770	176187970	0.05439	0.565
176188030	178909150	0.05597	0.648
178909210	181378210	0.05380	0.691
181378270	184105090	0.05633	0.424
184105090	186654250	0.05392	0.831
186654310	189381070	0.05256	0.702
189381070	191930230	0.05202	0.874
191930290	194656930	0.04959	0.918
194656990	197292010	0.05087	1.069
197292070	199932730	0.05651	0.560
199932790	202567750	0.05342	0.735
202567810	205208410	0.05449	0.633
205208470	207849070	0.05370	0.579
207849130	210713950	0.05605	0.452
213124570	215335510	0.05705	0.362
216017170	218228050	0.05514	0.414
218228110	220868530	0.05507	0.671
220868590	222145810	0.05276	0.719
225376210	226567510	0.05431	0.782

[a]Space craft (S/C) clock seconds. S/C clock is zero at *ROSAT* launch, 1990 June 1, 21:06:50 UT.

[b]HRI primary count rate (PCR) counts s^{-1} per PSPC MV counts s^{-1}.

[c]HRI PCR counts s^{-1} for $MV = 0$ counts s^{-1}.

Table 2. Observation details.

Parameter	Value
M101	–
Coordinates $(\alpha,\delta)_{2000}$	14^h 03^m $09\overset{s}{.}6$, 54° 20′ 24″
ROSAT Sequence	RH600383N00
PI	Wolfgang Pietsch
Exposure	32.62 ks
Observation Dates	1992 December 10 - 14
IC 2391	–
Coordinates $(\alpha,\delta)_{2000}$	8^h 41^m $40\overset{s}{.}8$, -52° 59′ 24″
ROSAT Sequence	RH201447N00
PI	Theodore Simon
Exposure	56.08 ks
Observation Dates	1994 May 13 - July 16
SMC #2	–
Coordinates $(\alpha,\delta)_{2000}$	0^h 57^m $12\overset{s}{.}0$, -72° 54′ 0″
ROSAT Sequence	RH600808A02
PI	Steven Snowden
Exposure	23.74 ks
Observation Dates	1997 April 3 - May 2
NGC 6822	–
Coordinates $(\alpha,\delta)_{2000}$	19^h 44^m $56\overset{s}{.}4$, $-14°$ 45′ 36″
ROSAT Sequence	RH600815A01
PI	Robert Petre
Exposure	52.85 ks
Observation Dates	1996 October 3 - 1996 October 9
Cygnus Loop - East	–
Coordinates $(\alpha,\delta)_{2000}$	20^h 57^m $16\overset{s}{.}8$, 31° 02′ 24″
ROSAT Sequence	RH500089A01
PI	John Raymond
Exposure	22.29 ks
Observation Dates	1991 November 5 - December 10

Table 3. Results.

Parameter	M101	IC 2391	SMC #2[a]	NGC 6822	Cygnus Loop
Total Counts (counts)	162404	242588	132028/132028	302282	872715
Accepted Counts (counts)	106527	157606	85150/82678	188689	697564
Channel Exclusion (counts)[b]	32875	49472	24559/24004	67835	76169
Radius Exclusion (counts)[c]	22803	33024	19633/19098	40013	82432
Exposure (ks)[d]	32.36	55.44	23.74/23.45	51.82	21.95
χ^2_ν of fit	1.06	1.19	1.57/1.32	1.26	2.94
Degrees of Freedom (ν)	1362	2359	1492/1474	3265	1070
Model PB Counts (counts)	180426	247955	136860/134317	341467	102015
Fitted Offset (counts s^{-1})	0.742	0.914	0.781/0.802	0.794	28.63
Fitted PB Model Scale Factor	0.477	0.465	0.497/0.489	0.441	0.376
Scaled PB Counts (counts)	85991	115182	67986/65668	150663	38348

[a]The values show the results before/after the exclusion of the atypical 301 s interval.

[b]Excluded events, PI channels ≤ 1 and ≥ 11.

[c]Excluded events, detector radius $> 17\farcm5$.

[d]Corrected for detector deadtime.

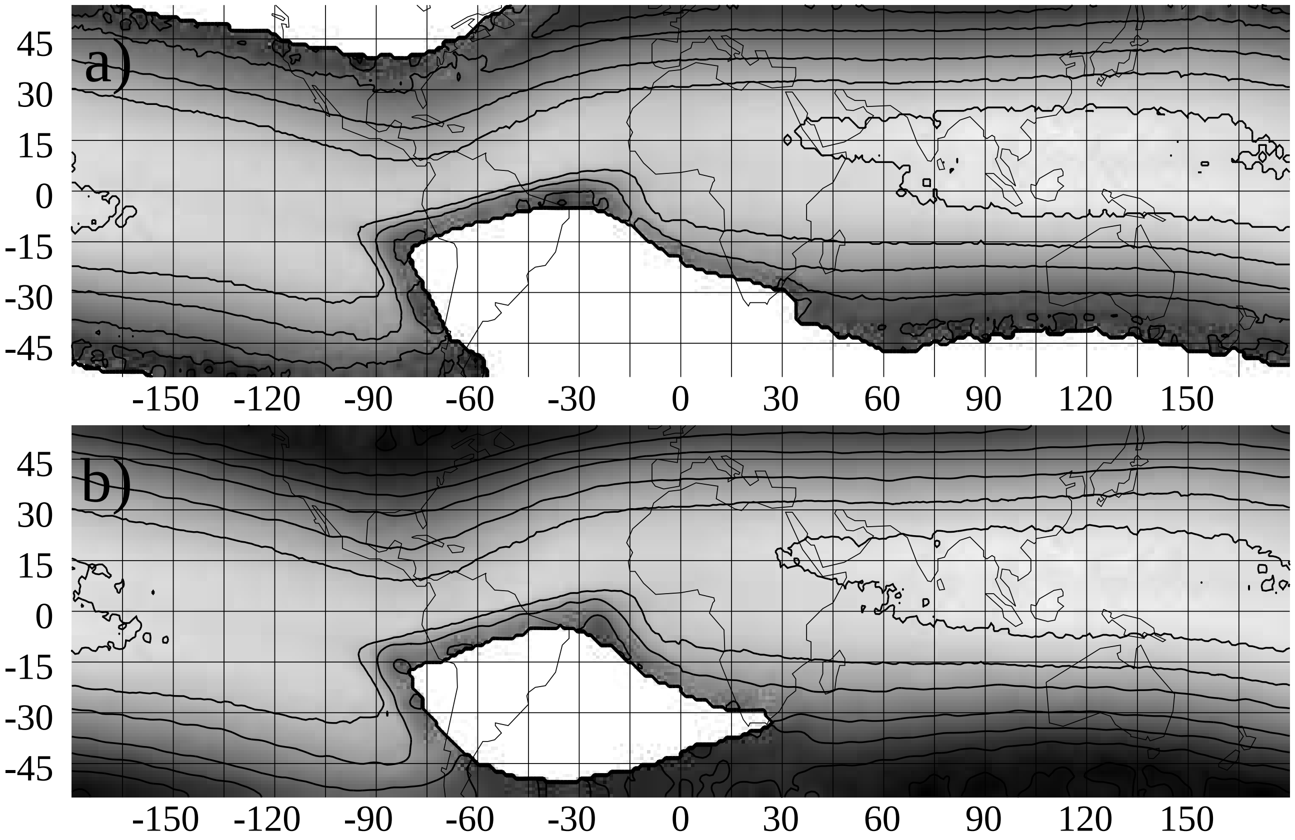
a)
45
30
15
0
-15
-30
-45
-150 -120 -90 -60 -30 0 30 60 90 120 150
b)
45
30
15
0
-15
-30
-45
-150 -120 -90 -60 -30 0 30 60 90 120 150

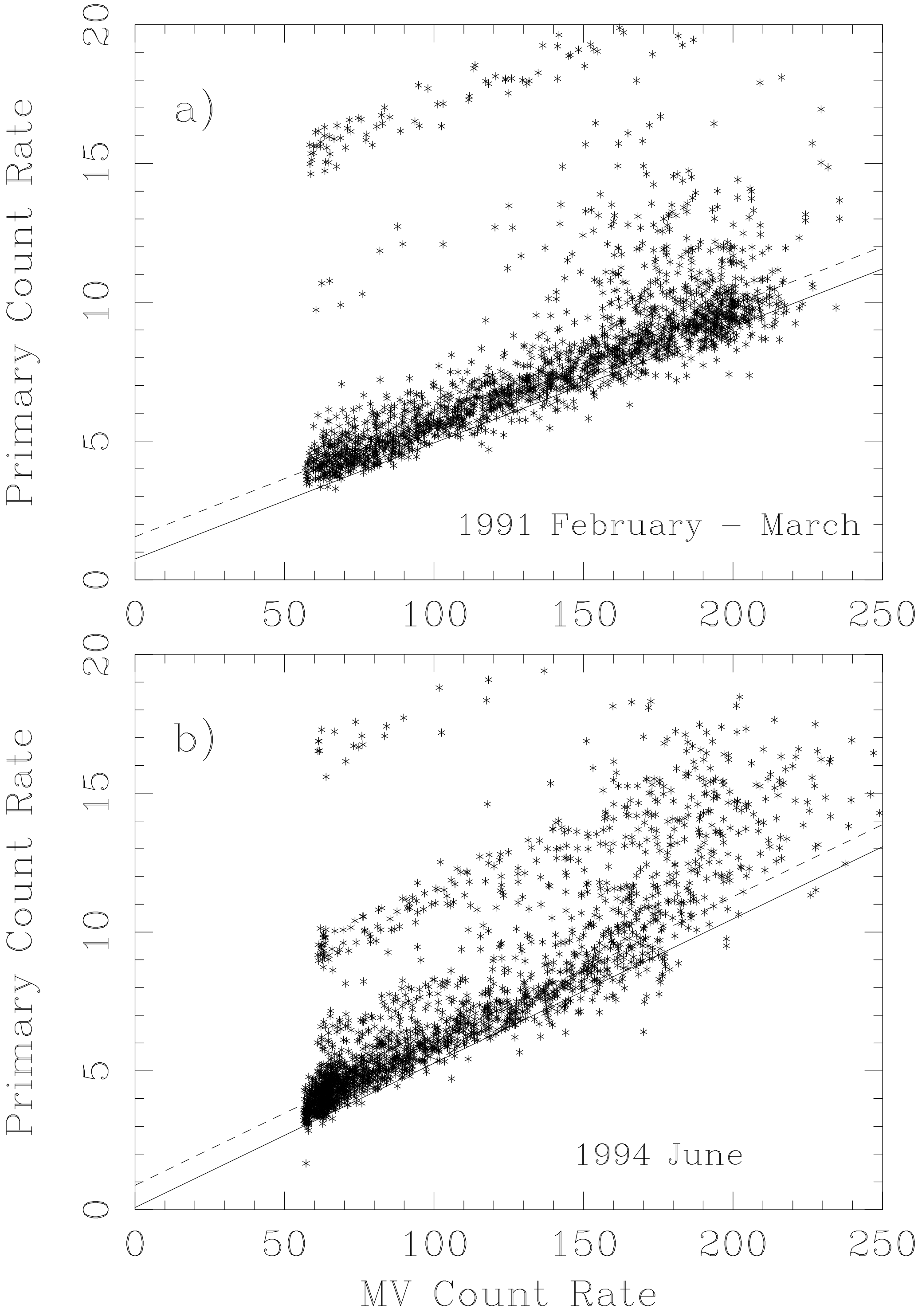
a)
1991 February – March
b)
1994 June
Primary Count Rate
Primary Count Rate
MV Count Rate
0
5
10
15
20
0
50
100
150
200
250

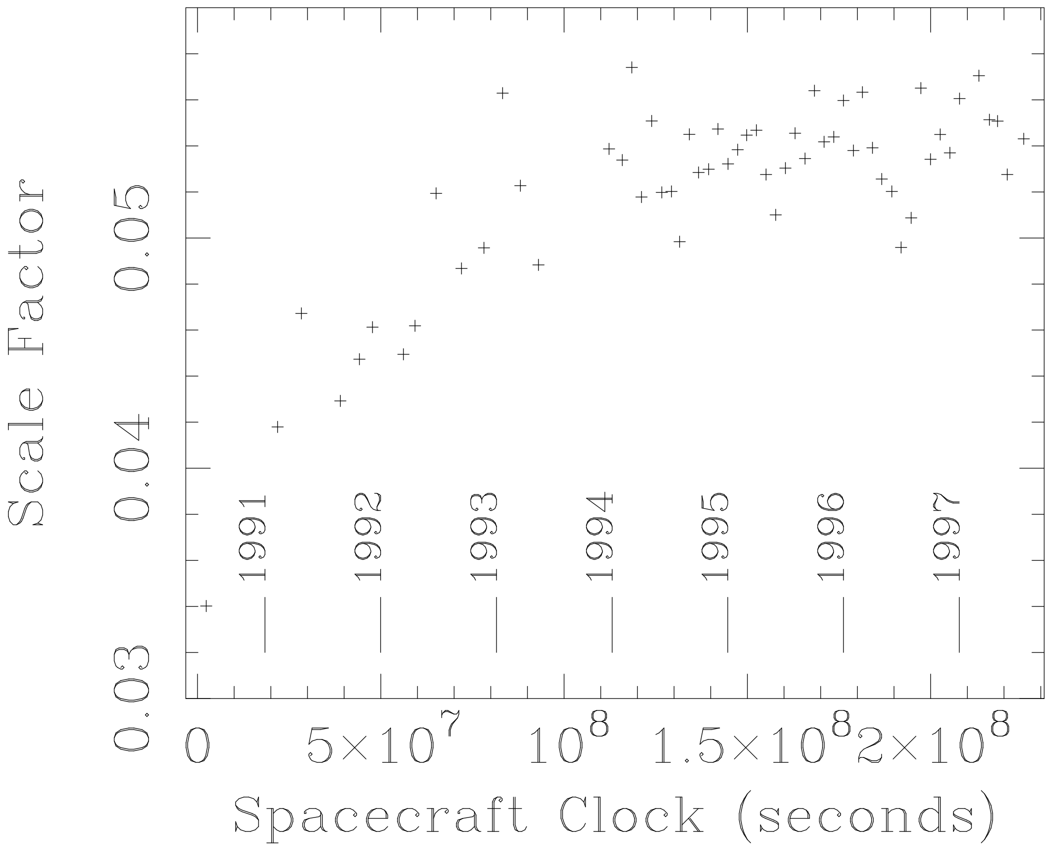
Scale Factor
0.03
0.04
0.05
0
5×10^7
10^8
1.5×10^8
2×10^8
Spacecraft Clock (seconds)
1991
1992
1993
1994
1995
1996
1997

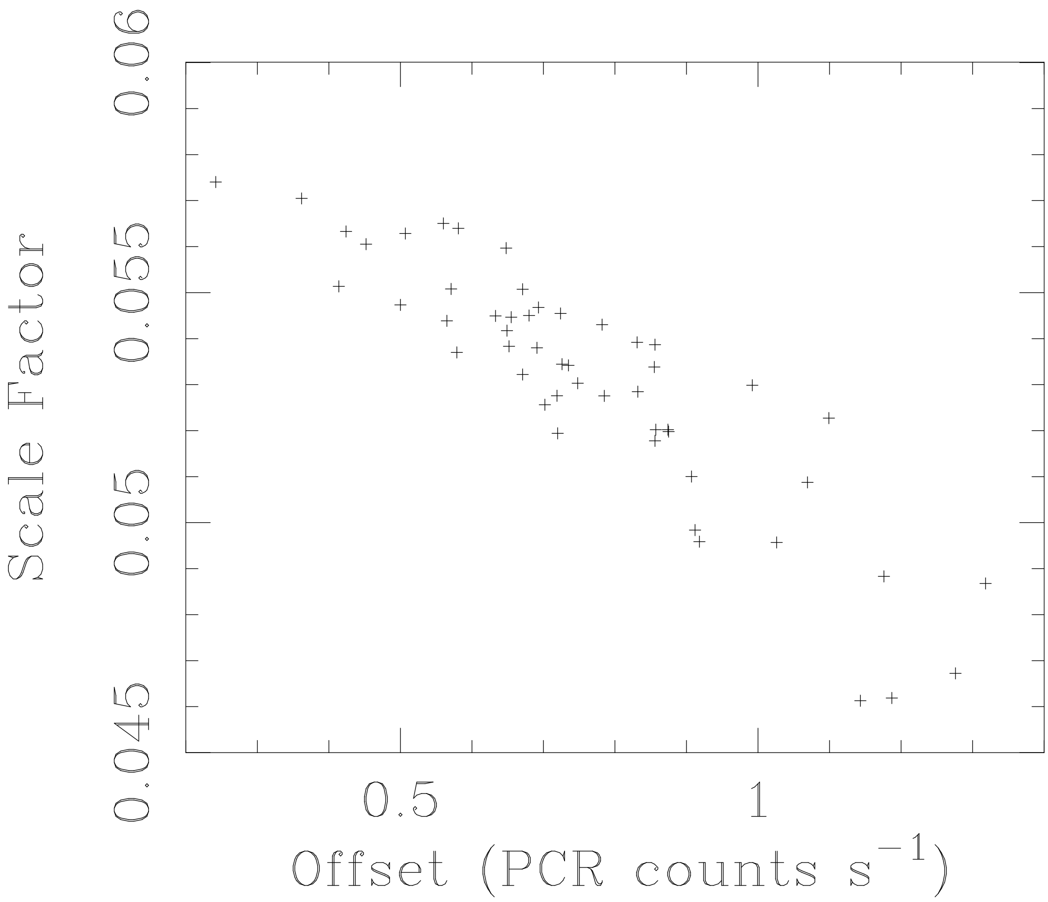
0.045
0.05
0.055
0.06
Scale Factor
0.5
1
Offset (PCR counts s^{-1})

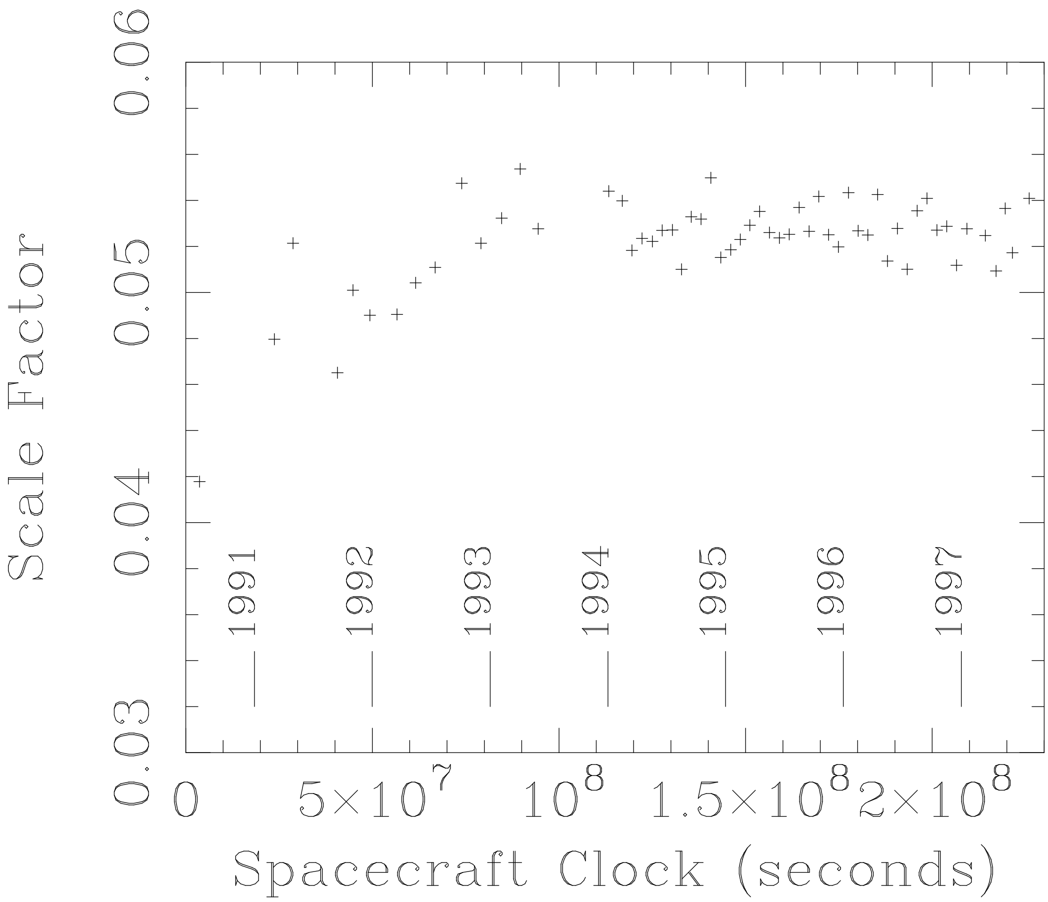
Scale Factor
0.03
0.04
0.05
0.06
0
5×10^7
10^8
1.5×10^8
2×10^8
Spacecraft Clock (seconds)
1991
1992
1993
1994
1995
1996
1997

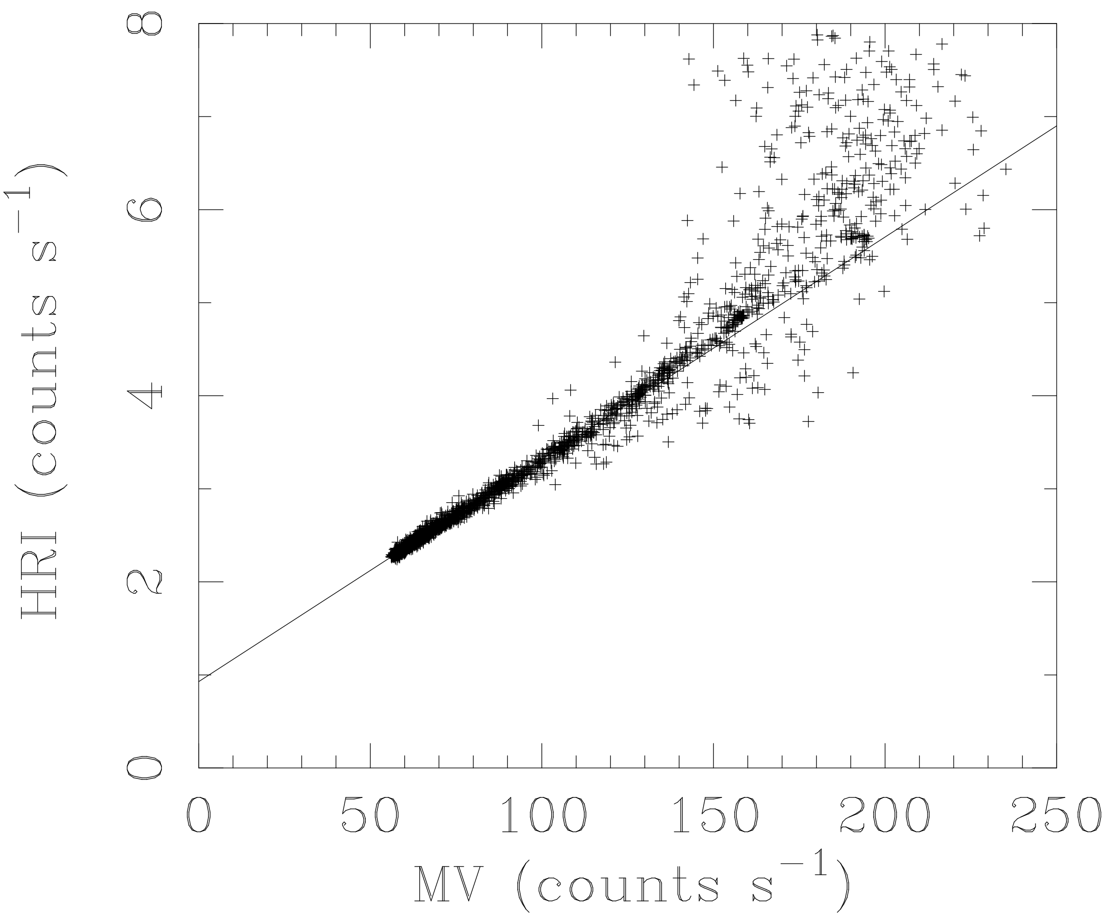

HRI (counts s^{-1})
MV (counts s^{-1})
0
2
4
6
8
0
50
100
150
200
250

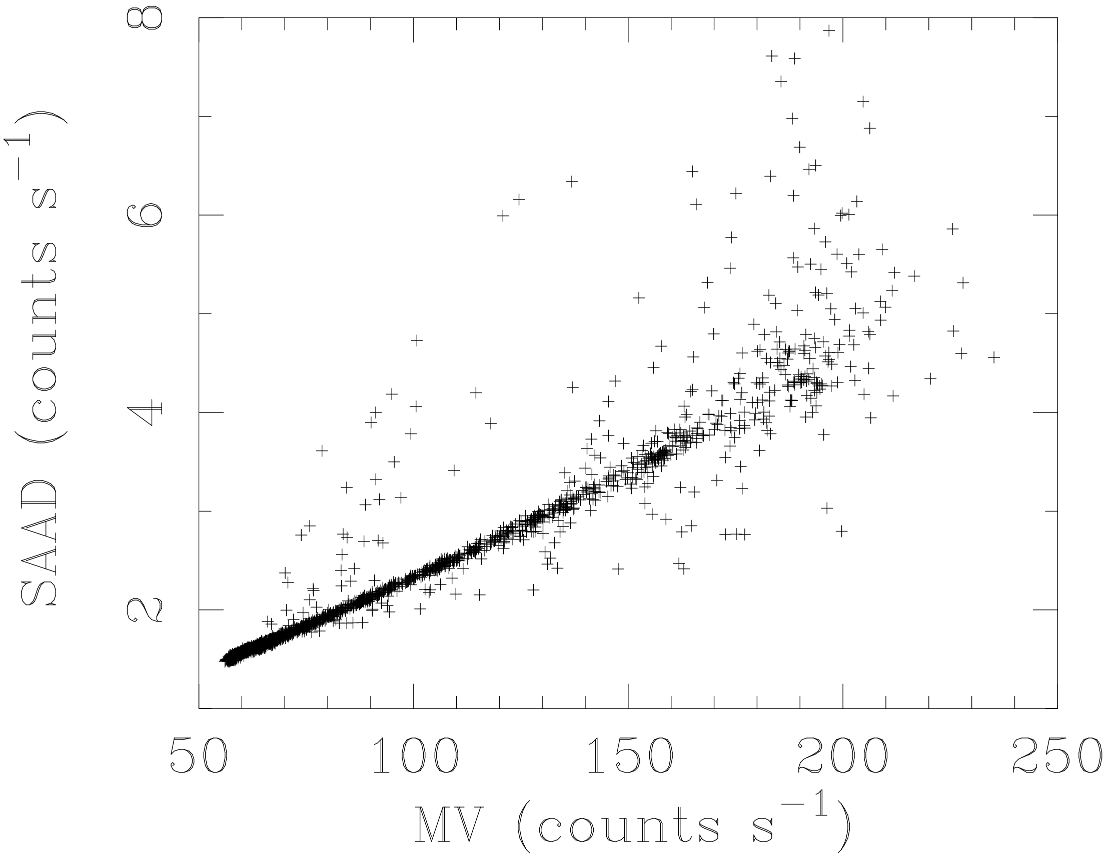
8
6
4
2
SAAD (counts s^{-1})
50
100
150
200
250
MV (counts s^{-1})

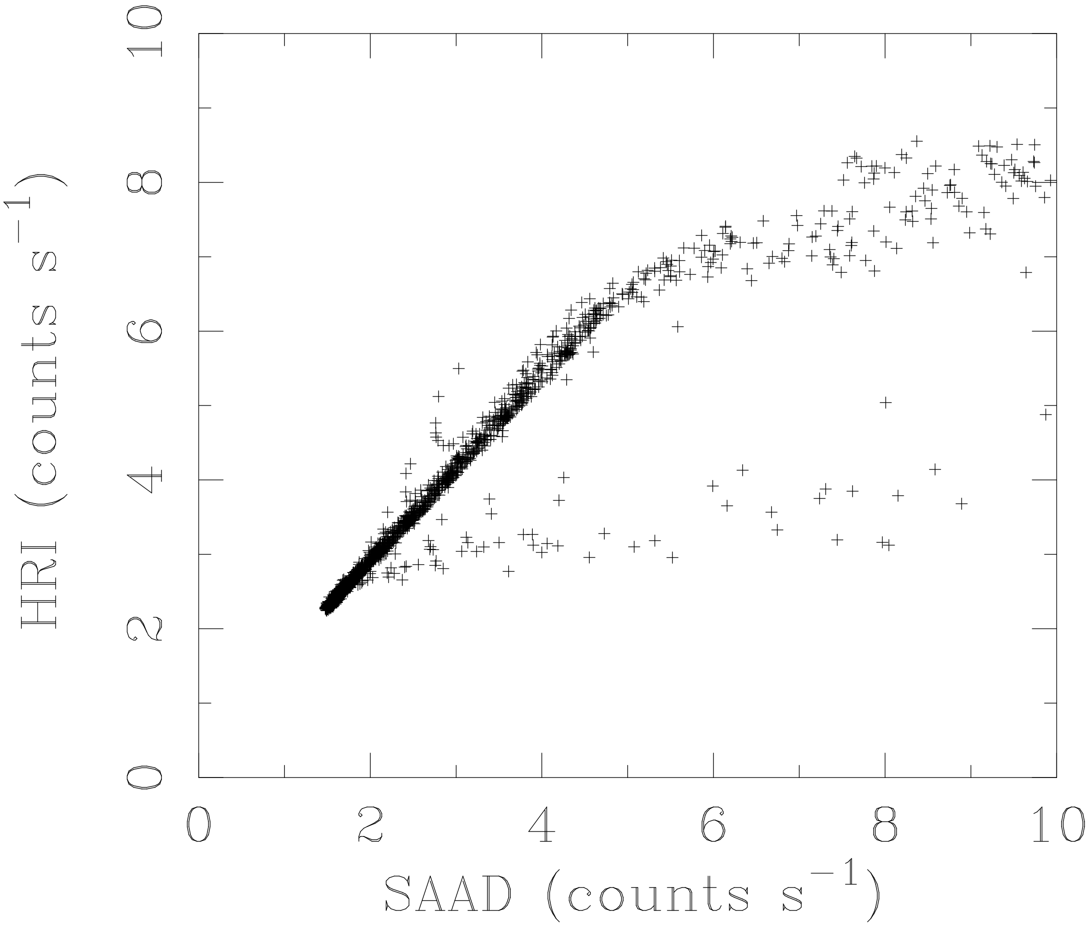
HRI (counts s^{-1})
SAAD (counts s^{-1})
0
2
4
6
8
10
0
2
4
6
8
10

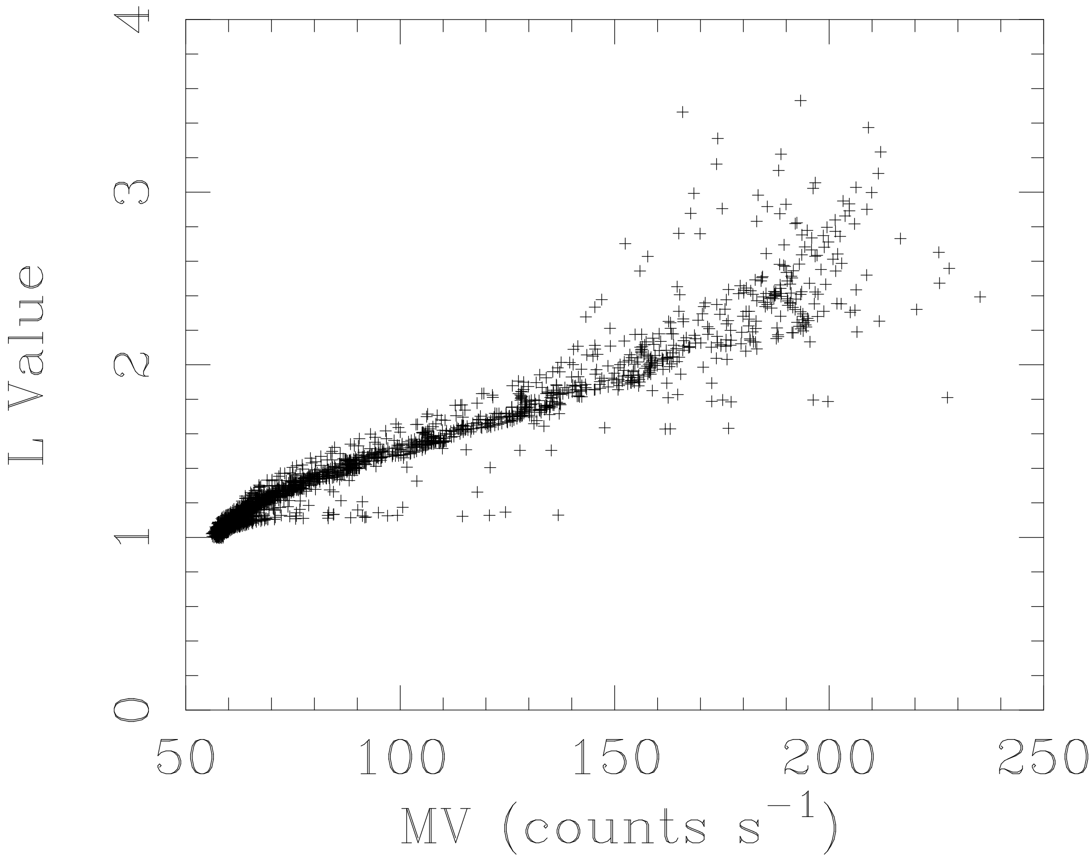
L Value
MV (counts s^{-1})
0
1
2
3
4
50
100
150
200
250

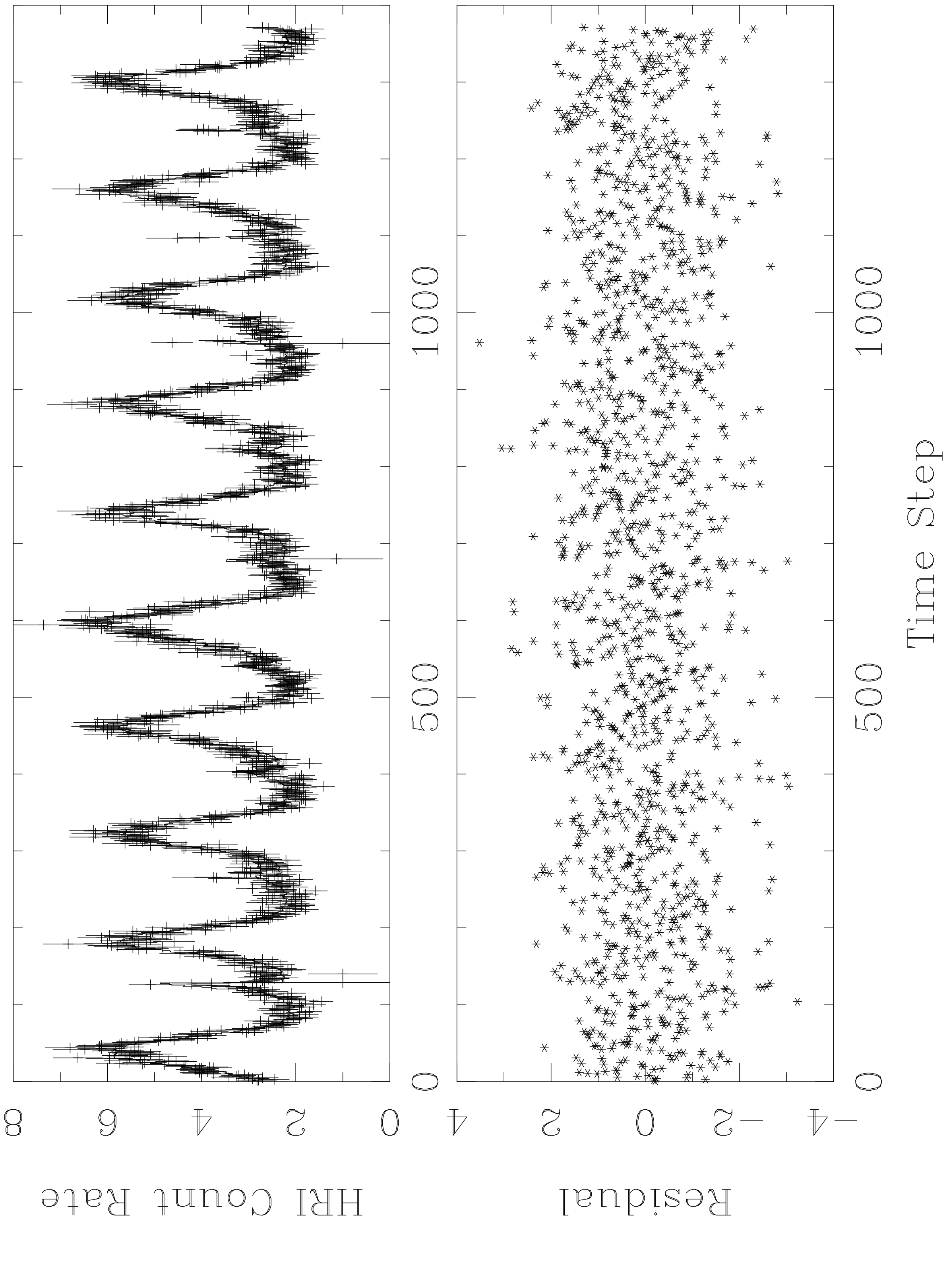
HRI Count Rate
0
2
4
6
8
Residual
−4
−2
0
2
4
Time Step
0
500
1000

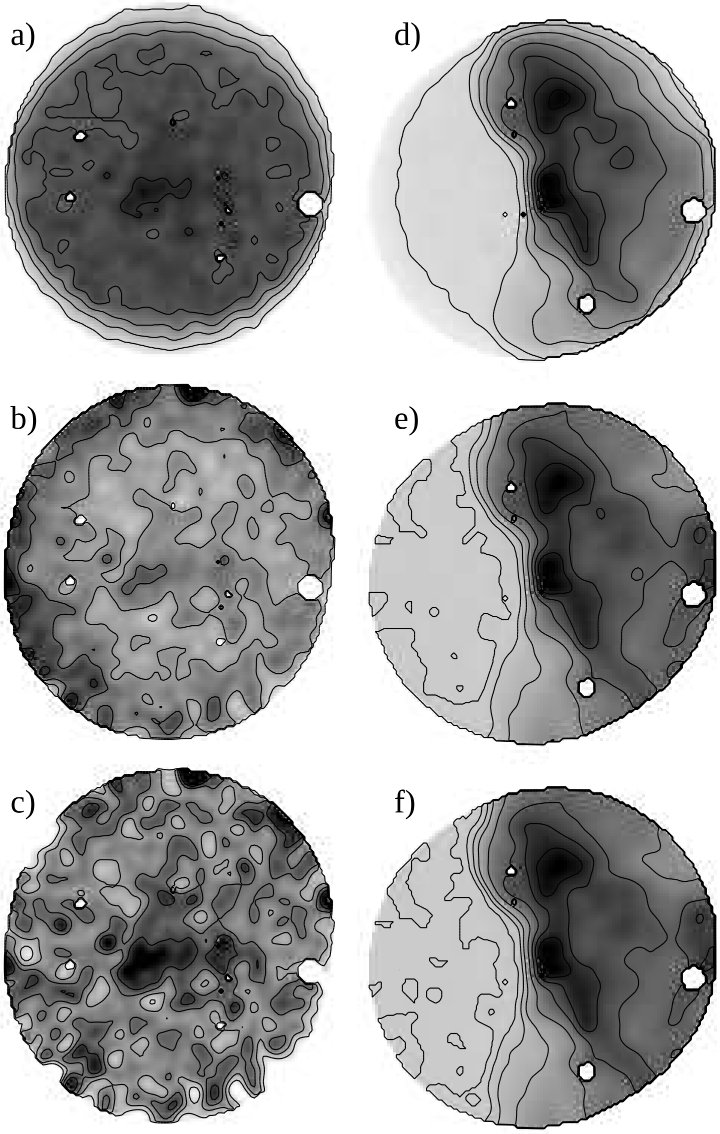

a)
d)
b)
e)
c)
f)

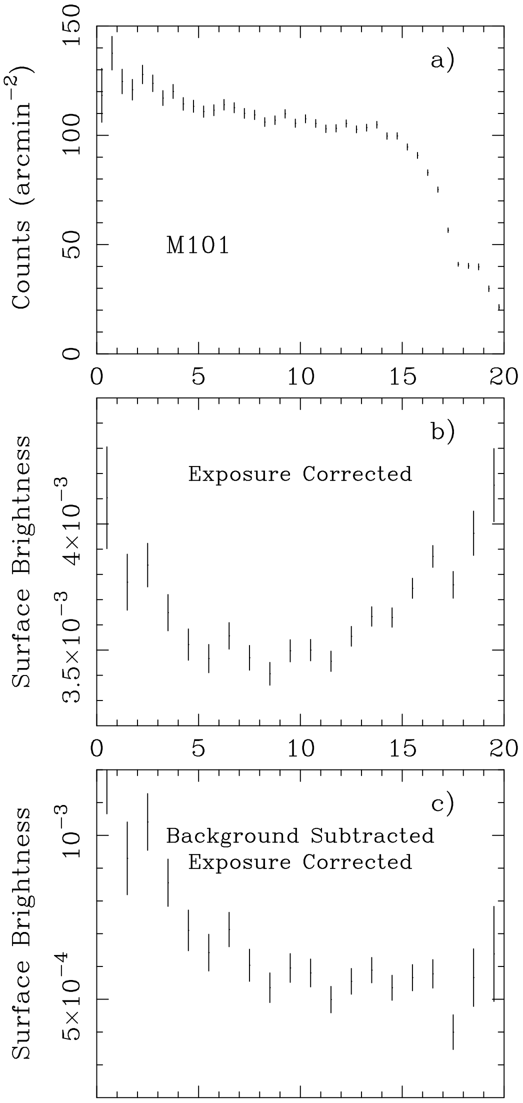

a)
M101
Counts (arcmin^{-2})
0
50
100
150
0
5
10
15
20
b)
Exposure Corrected
Surface Brightness
3.5×10^{-3}
4×10^{-3}
0
5
10
15
20
c)
Background Subtracted
Exposure Corrected
Surface Brightness
5×10^{-4}
10^{-3}
0
5
10
15
20
Radius (arcmin)

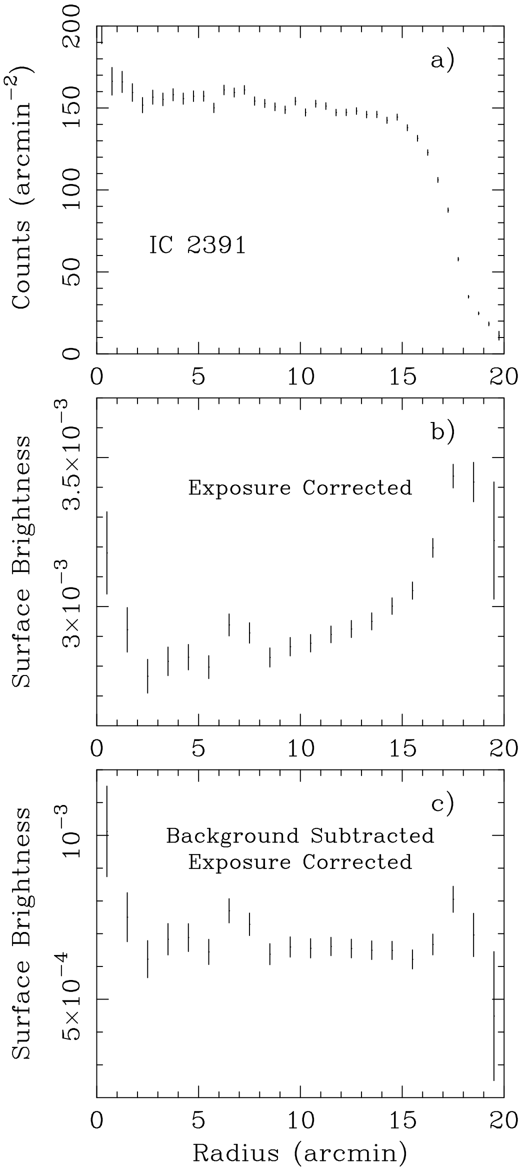
a)
IC 2391
Counts (arcmin^{-2})
b)
Exposure Corrected
Surface Brightness
c)
Background Subtracted
Exposure Corrected
Surface Brightness
Radius (arcmin)

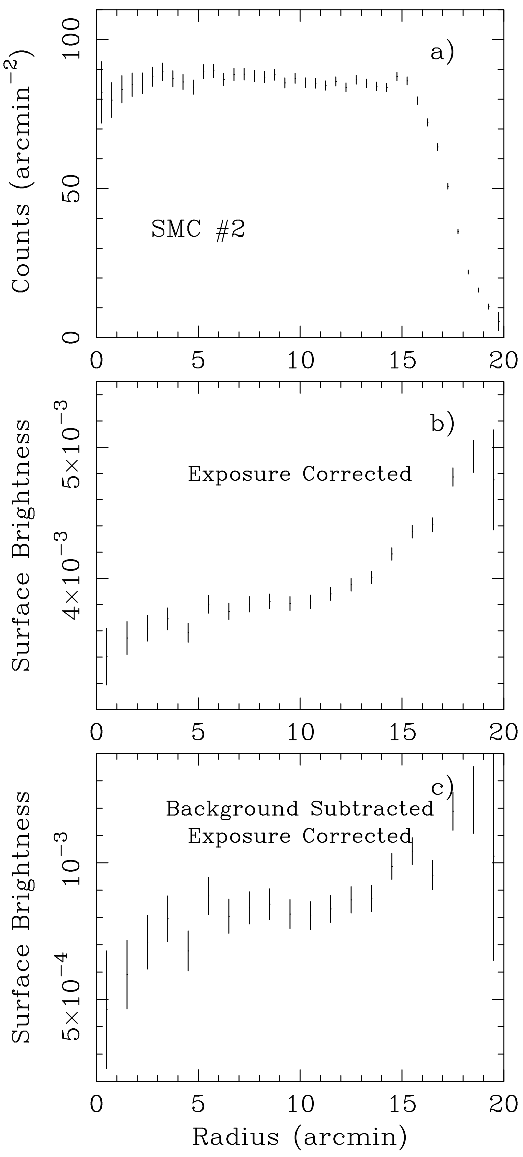
a)
SMC #2
Counts (arcmin^{-2})
0
50
100
b)
Exposure Corrected
Surface Brightness
4×10^{-3}
5×10^{-3}
c)
Background Subtracted
Exposure Corrected
Surface Brightness
5×10^{-4}
10^{-3}
0
5
10
15
20
Radius (arcmin)

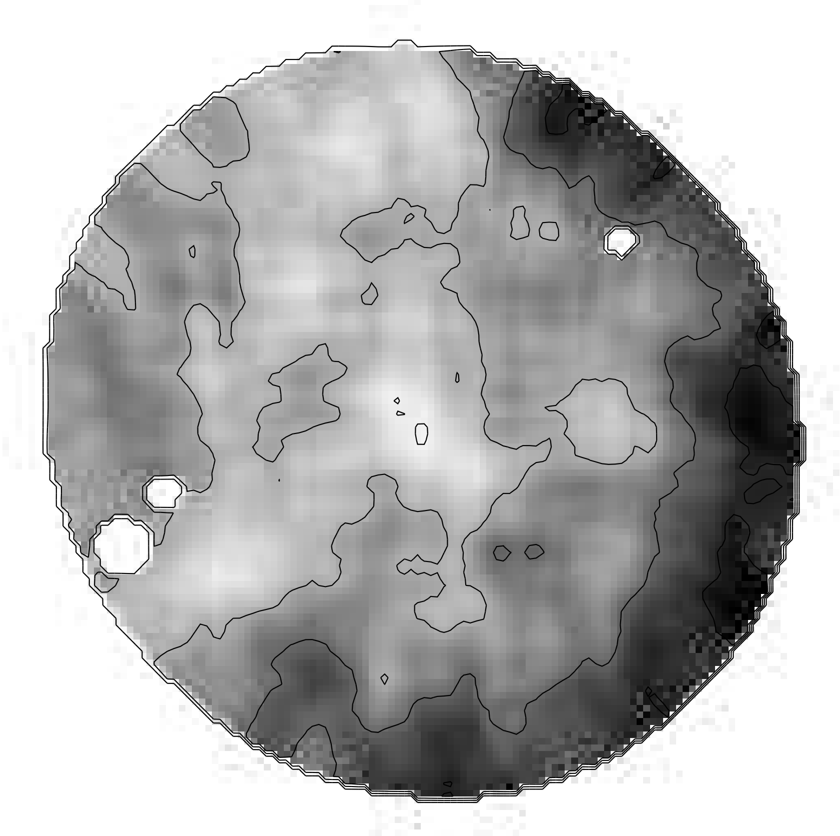

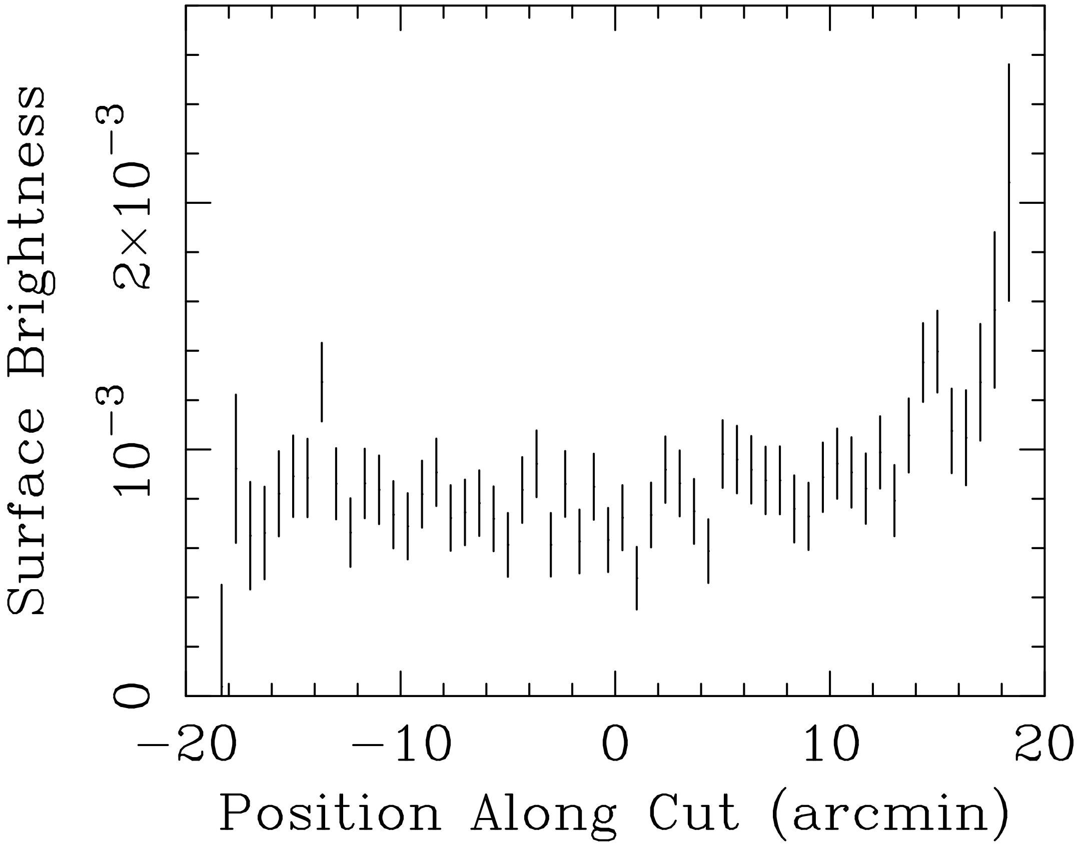

Surface Brightness
0
10^{-3}
2×10^{-3}
−20
−10
0
10
20
Position Along Cut (arcmin)

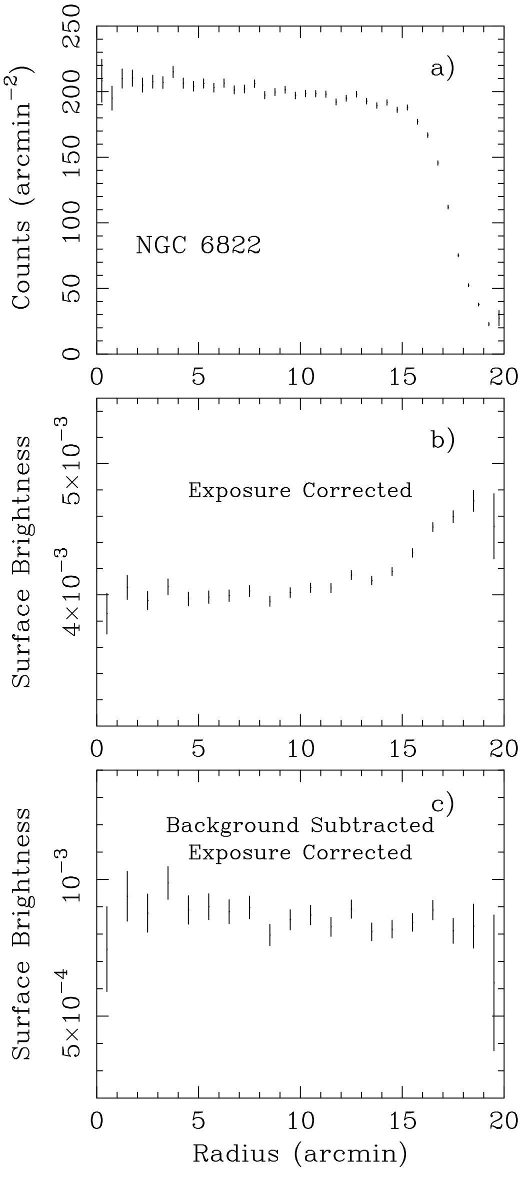
a)
NGC 6822
Counts (arcmin^{-2})
0
50
100
150
200
250
0
5
10
15
20
b)
Exposure Corrected
Surface Brightness
4×10^{-3}
5×10^{-3}
0
5
10
15
20
c)
Background Subtracted
Exposure Corrected
Surface Brightness
5×10^{-4}
10^{-3}
0
5
10
15
20
Radius (arcmin)

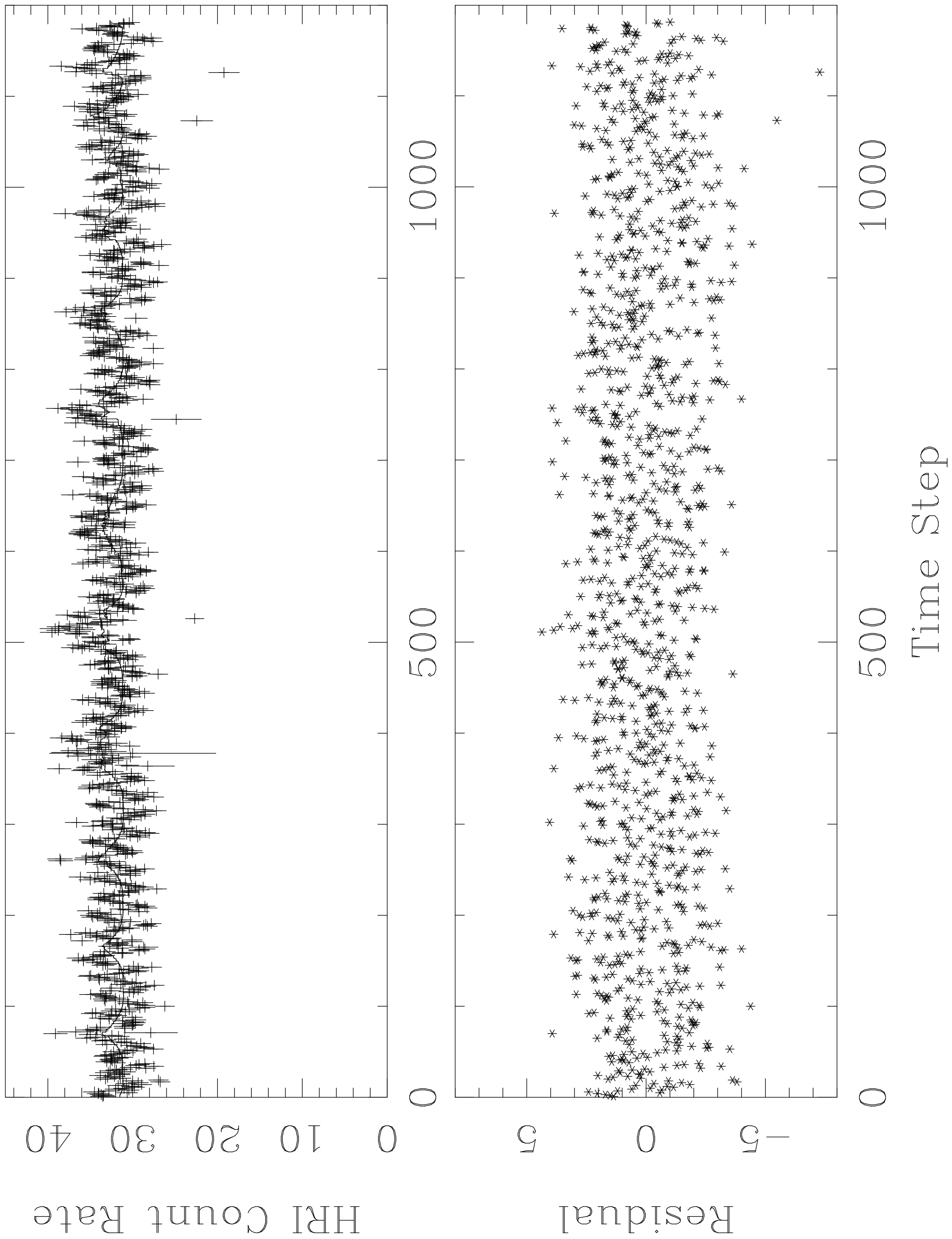
HRI Count Rate
40
30
20
10
0
Residual
5
0
−5
Time Step
0
500
1000

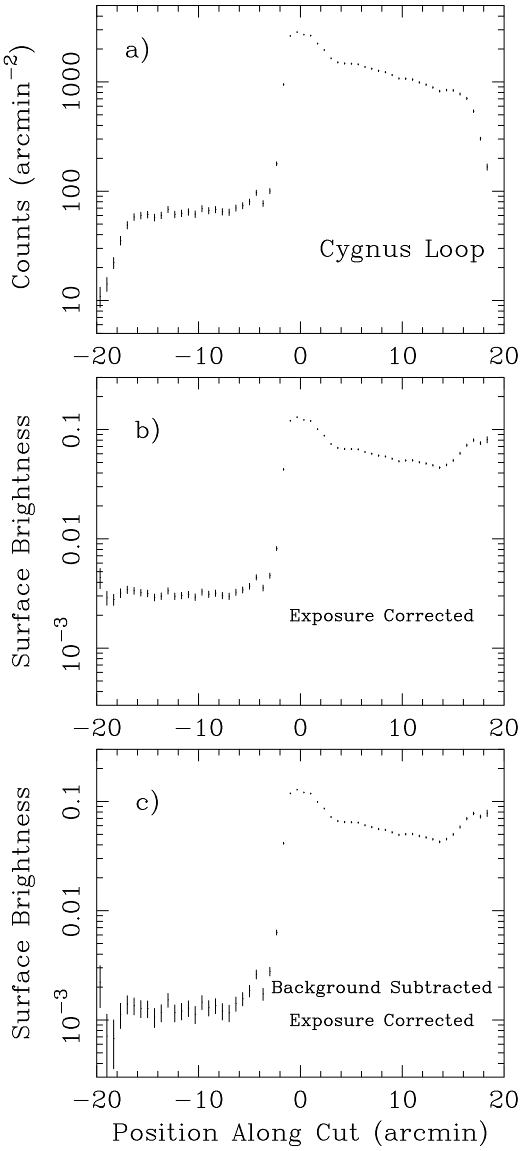

a)
Cygnus Loop
Counts (arcmin^{-2})
1000
100
10
−20
−10
0
10
20
b)
Exposure Corrected
Surface Brightness
0.1
0.01
10^{-3}
c)
Background Subtracted
Exposure Corrected
Position Along Cut (arcmin)